Research Square

Preprints are preliminary reports that have not undergone peer review.
They should not be considered conclusive, used to inform clinical practice,
or referenced by the media as validated information.

Designing and Modelling of an Induction Motor Using Advanced High-Temperature Materials for Extremely Harsh Industrial Applications

Asuquo Eke

ekeasuquo@gmail.com

Cross River State University of Technology: Cross River University of Technology
https://orcid.org/0009-0000-9576-2910

Research Article

Keywords: Induction motor, High-temperature materials, ANSYS Motor-CAD, Finite Element Analysis, Harsh environments and thermal management, High-temperature insulation

Posted Date: November 26th, 2026

DOI: https://doi.org/10.21203/rs.3.rs-11861994/v1

License: This work is licensed under a Creative Commons Attribution 4.0 International License.
Read Full License

Additional Declarations: The authors declare no competing interests.

DESIGNING AND MODELLING OF AN INDUCTION MOTOR USING ADVANCED HIGH-TEMPERATURE MATERIALS FOR EXTREMELY HARSH INDUSTRIAL APPLICATIONS

Asuquo Eke[1], Ake, David, Archibong Etim, O.I. Okoro[2]

Department of Electrical/Electronic Engineering, Cross River University of Technology, Calabar. Nigeria
Department of Electrical/Electronic Engineering Admiralty University of Nigeria, Delta State. Nigeria
Department of Electrical and Electronic Engineering, Michael Okpara University of Agriculture, Umudike. Abia State. Nigeria
*Department of Electrical and Electronic Engineering, Michael Okpara University of Agriculture, Umudike. Abia State. **Nigeria***
Department of Electrical/Electronic Engineering, Cross River University of Technology, Calabar. Nigeria
* Correspondence: ekeasuquo@gmail.com, (+234-7039102495)
Corresponding author, **Asuquo Eke[1]:** *Cross River University of Technology, Calabar. Nigeria*

Abstract

A typical induction motor is subjected to temperatures of over 300 °C, thermal stresses, exposure to various corrosive media, and heavy mechanical overloads in a industrial environment leading to rapid insulation degradation, increased losses, reduced efficiency and limited-service life. The design and multiphysics analysis of a 1.5 kW, 380 V, 50 Hz, four-pole, three-phase squirrel-cage induction motor using cutting-edge high-temperature materials are described in this paper. Hiperco 50A cobalt-iron laminations, oxygen-free copper rotor bars, polyimide-ceramic insulation, an Inconel 718 shaft, and silicon-nitride hybrid bearings are some of the proposed motor's characteristics. ANSYS Maxwell and Motor-CAD software were utilized to perform coupled electromagnetic-thermal analysis, which combined finite element analysis with a lumped parameter thermal network. The proposed design provides a peak air-gap flux density of 1.18 T, a starting torque of 22.6 Nm, a maximum torque of 27.3 Nm, and an efficiency of 92.6% compared to the conventional motor's 88.2% of efficiency. Torque ripple was reduced from 7.8% to 2.4%, while overall losses were reduced by 22.3%, and the temperature of the winding hotspot was reduced from 278 °C to 176 °C. These results suggest that the new induction motor has improved electromagnetic characteristics, thermal endurance, efficiency, and reliability in high-temperature industrial environments.

Keywords: Induction motor, High-temperature materials, ANSYS Motor-CAD, Finite Element Analysis, , Harsh environments and thermal management, High-temperature insulation

1. Introduction

Industrial electrification has been one of the main pillars in the development of global manufacturing, mining, transportation, petrochemical processing, metallurgy and power generation. Among all industrial electric machines, the three-phase squirrel-cage induction motor remains the most used due to its rugged construction, relatively low manufacturing cost, high reliability, ease of maintenance and satisfactory operational efficiency. Induction motors account for approximately 70% of industrial electrical energy consumption worldwide and continue to dominate the medium- and high-power industrial applications due to their robustness and operating simplicity [1, 2]. Electric equipment which can function in extremely severe environment is becoming more and more necessary for the modern industry. Electric motors are often exposed to ambient temperatures above 250-300 °C, aggressive corrosive chemicals, abrasive dust particles, moisture intrusion, intense mechanical vibration, and long-time continuous-duty operation in the areas such as steel rolling mills, aluminium smelters, cement kilns, geothermal energy plants, underground mining systems, offshore oil and gas platforms, aerospace propulsion auxiliaries, nuclear facilities, and chemical processing plants. In the end, these severe operating circumstances shorten the machine's operational lifespan and reliability by greatly accelerating thermal aging and insulation breakdown [3, 5]. Temperature is recognized to be the most critical factor affecting induction motor reliability. According to the Arrhenius thermal aging principle, every 10 °C increase over the rated insulation temperature approximately halves the insulation life expectancy. Excessive operating temperatures degrade dielectric strength, reduce winding insulation resistance, accelerate oxidation of metallic components, increase bearing wear, and promote irreversible material degradation. Consequently, thermal failure accounts nearly 40-60% of the induction motor breakdowns reported in the industrial sector [6, 7]. Traditional induction motors are commonly designed by using silicon steel laminations, electrolytic copper conductors, cast aluminium rotors and Class F or Class H insulation systems with maximum allowable temperatures of 155 °C and 180 °C, respectively. Although these materials are adequate for the general industrial environments, they become inappropriate for the continuous operation in high-temperature applications. Elevated temperatures increase the electrical resistivity of copper windings, consequently, increasing the Joule losses, reducing efficiency, lower torque

production and power factor. Simultaneously, magnetic materials experience increased core losses and reduced permeability while the conventional lubricants and rolling-element bearings degrade prematurely [8, 9]. To circumvent the above limitations, recent developments in material science offer a new generation of high-temperature engineering materials suitable for the electric machine construction. These materials include cobalt-iron magnetic alloys with better saturation flux density, nickel-based superalloys with outstanding mechanical strength at high temperatures, ceramic electrical insulators with excellent dielectric stability, silicon nitride hybrid bearings with low-friction and high thermal resistance, polyimide-based insulation systems with the ability to operate continuously above 300 °C, and high-performance thermal interface materials for improved heat dissipation [10, 13]. Induction motors can now function dependably in situations that were previously thought to be unfeasible for traditional machine designs because to the integration of these cutting-edge materials. Electric machine design techniques have also been improved by concurrent advancements in computational engineering. Accurate forecasts of flux distribution, torque ripple, magnetic saturation, eddy-current losses, and electromagnetic forces are made possible by the comprehensive electromagnetic field solutions provided by contemporary finite element analysis (FEA) techniques like ANSYS Maxwell. Similarly, ANSYS Motor-CAD enables rapid evaluation of the thermal performance via a lumped parameter thermal network (LPTN) modelling approach to accurately estimate the temperature distribution in the stator windings, rotor bars, shaft, housing, and bearings. Coupling electromagnetic and thermal simulations gives a comprehensive understanding of the motor performance under severe thermal loading [14, 17]. Despite this technological advancement, few studies have addressed the integrated design of the induction machines particularly intended for continuous operation above 300 °C using the advanced high-temperature materials. Moreover, most of the previous works have been concentrated either on the electromagnetic or thermal aspects without considering the influence of the high-temperature material choice on the overall performance. Comprehensive design methodologies incorporating electromagnetic analysis, thermal modelling, structural considerations and material optimization are still limited.

This study presents the complete design and the multiphysics modelling of a three-phase squirrel-cage induction motor utilizing the advanced high-temperature materials for extremely harsh industrial applications. A coupled electromagnetic-thermal modelling framework based on ANSYS Motor-CAD and ANSYS Maxwell is developed to study the magnetic performance, temperature distribution and heat transfer characteristics of the machine. The objective is to retain high efficiency at high ambient temperatures while increasing thermal endurance, reducing temperature rise, improving operational reliability, and extending service life. Due to developments in the aerospace, renewable energy, military, geothermal, mining, and heavy industrial sectors, the need for electric machines that can operate at high temperatures has grown dramatically over the past 20 years. Conventional induction motors are generally designed for ambient temperatures below 40 °C with insulation systems limiting the winding temperatures to about 155-180 °C. However, industrial environments such as geothermal drilling, steel production and nuclear reactors require motors to be able to operate continuously at a much higher temperature. The primary goal of early research on high-temperature motors was to enhance the insulating system. To increase dielectric strength at high temperatures, glass-fiber composites, silicone varnishes, mica tapes, and class H insulation were introduced. Although these approaches improved the thermal endurance, they did not address the issues of thermal expansion mismatch, magnetic property degradation and bearing reliability under prolonged high-temperature exposure [18, 19]. Polyimide insulation systems, ceramic-coated conductors, and inorganic insulating materials that can operate continuously beyond 300 °C were introduced by later innovations. For demanding industrial applications, these materials demonstrated enhanced dielectric performance and thermal stability [20].

B. Advanced Magnetic Materials

The magnetic core materials largely govern the efficiency and power density of induction motors. At typical operating temperatures, conventional non-oriented silicon steel has good magnetic characteristics; but, at higher temperatures, its permeability decreases and its core losses increase. To get around these restrictions, researchers have looked into cobalt-iron alloys, amorphous magnetic materials, and nanocrystalline alloys. Cobalt-iron alloys offer high saturation flux density (≈2.35 T), excellent mechanical strength, and improved thermal stability making them attractive for aerospace and high-temperature electric machines. Amorphous alloys offer significantly lower core losses but face manufacturing challenges due to brittle nature and high cost. Nanocrystalline materials combine low losses with excellent permeability although their commercial application is limited [19, 20].

C. High-temperature Conductors and Rotor Materials

Copper remains the preferred conductor for induction motor windings due to its high electrical conductivity. However, increasing temperature results in increased electrical resistivity of copper, hence, increasing the copper losses under harsh operating conditions. Researchers have investigated oxygen-free high-conductivity copper, silver-alloy conductors and advanced copper alloys for enhanced thermal stability. From traditional cast aluminum to copper rotors and nickel-based superalloys that show exceptional mechanical strength and resistance to oxidation at high temperatures, rotor cage materials have changed over time. These materials lessen thermal distortion during extended operation and increase the rotor's durability [20]. Although considerable advancements have been made in the area of induction motor design, most of the existing studies focus primarily on improving efficiency, reducing losses, enhancing torque density or optimizing the electromagnetic

performance under standard industrial operating conditions. Very limited research has addressed the comprehensive design of induction motors for continuous operation in environments where ambient temperatures exceed 300 °C coupled with corrosive chemicals, abrasive particles, severe mechanical vibrations and restricted cooling conditions. Most commercial induction motors continue to use conventional silicon steel laminations, Class F or H insulation systems, aluminium rotor cages and standard rolling bearings. These materials experience significant degradation under prolonged exposure to elevated temperatures due to increased oxidation, thermal expansion, insulation aging, and mechanical fatigue. Few investigations have explored the advanced materials such as Cobalt-Iron magnetic alloys, Nickel-based superalloys, Ceramic electrical insulation, Silicon nitride bearings, Polyimide insulation and High-temperature epoxy composites. However, these studies investigate the individual materials rather than their combined influence on the overall motor performance. Most published work investigates either electromagnetic performance or thermal performance independently. Since, the electromagnetic losses directly generate heat which subsequently modifies the electric conductivity, magnetic permeability, winding resistance and machine efficiency, these separate analyses cannot accurately predict the real industrial operation. A fully coupled electromagnetic-thermal framework is relatively scarce. Many thermal investigations consider operating temperatures below 180°C because they correspond to Class H insulation systems. Industrial sectors such as geothermal drilling, steel manufacturing, aerospace propulsion and nuclear processing require machines that are capable to operate reliably beyond 300°C.

2. Materials and methods

The proposed methodology combines analytical motor design with finite element electromagnetic analysis and lumped parameter thermal modeling.

2.1 Proposed Motor Specifications

Table 1 summarizes the design specifications.

Table I: Motor Design Parameters

Parameter	Value
Motor Type	Three-Phase SCIM
Rated Power	1.5 kW
Rated Voltage	380 V
Rated Frequency	50 Hz
Rated Speed	1450 rpm
Number of Poles	4
Rotor Type	Squirrel Cage
Rotor Bars	24
Stator Slots	28
Cooling	Air Cooling / Optional Water Jacket
Efficiency Target	>92%
Ambient Temperature	300–350°C
Insulation Class	Advanced Polyimide Ceramic

2.2 HIGH-TEMPERATURE MATERIAL SELECTION

One of the most important parts of the suggested design is the choice of materials since every machine component needs to be able to tolerate high temperatures while still having appropriate mechanical and electrical characteristics. The suggested design uses Hiperco 50A (Cobalt-Iron Alloy) for stator core materials rather than traditional M19 silicon steel. Benefits include reduced magnetic saturation, minimal hysteresis loss, improved thermal stability, high saturation flux density (≈2.35 T), and good permeability. Conventional die-cast aluminium is replaced with oxygen-free high-conductivity copper for rotor cage material. Improved starting torque, lower electrical resistance, lower rotor copper losses, and higher efficiency are some advantages. Inconel 718, a nickel-based superalloy with exceptional fatigue performance, high tensile strength, great oxidation resistance, and outstanding creep resistance, is used to make the shaft. The proposed insulation consists of Polyimide enamel, Ceramic mica tape, and glass fiber reinforcement, with a maximum continuous operating temperature of 380°C. Bearings use Silicon nitride hybrid ceramic bearings are selected because they exhibit a low friction coefficient, high hardness, excellent wear resistance, corrosion resistance, and high-speed capability. Cast stainless steel is used to make the housing, which has built-in cooling fins for improved heat dissipation.

2.3 ELECTROMAGNETIC DESIGN PROCEDURE

The proposed induction motor is designed according to classical electrical machine design theory before validation using finite element simulation. The output power of an induction motor is expressed as

$$P = C_0 D^2 L n \quad (1)$$

Where P is the output Power (kW), D is the stator bore diameter (m), L is the Core Length (m), n is the Speed (rps), C_o = Output coefficient, and the output coefficient is

$$C_0 = 11 K_w B_{av} a_c \times 10^{-3} \quad (2)$$

where K_w is the winding factor, B_{av} is the average air-gap flux density, and a_c is the Specific electric loading
The air-gap flux per pole is

$$\Phi = B_{av} T l \quad (2)$$

Where $\tau = \frac{\pi D}{P}$
Specific electric loading is given by equation (3)

$$a_c = \frac{IZ}{\pi D} \quad (3)$$

Where I is the Current and Z is the Total conductors
The required number of turns per phase is

$$T = \frac{E}{4.44 f K_w \Phi} \quad (4)$$

Where E = Phase voltage and f is the frequency, and the magnetizing current is estimated as

$$I_m = \frac{B_g l_g}{\mu_0 N} \quad (5)$$

For air-gap length, **t**he empirical air-gap equation becomes

$$g = 0.2 + 2\sqrt{DL}\ (\text{mm}) \quad (6)$$

For the proposed motor, the air-gap is 0.45–0.50 mm, which offers an optimal compromise between
Torque, efficiency, leakage reactance, and thermal behavior. [21]
The total motor losses are

$$P_{loss} = P_{cu,s} + P_{cu,r} + P_{core} + P_{fw} + P_{stray} \quad (7)$$

Where Stator copper loss, Rotor copper loss, Iron loss, and Mechanical loss are given in equations 8-11.

$$P_{cu,s} = 3 I^2 R_s \quad (8)$$
$$P_{cu,r} = 3 I_r^2 R_r \quad (9)$$
$$P_{core} = P_h + P_e \quad (10)$$
$$P_{fw} = P_f + P_w \quad (11)$$

2.4. ELECTROMAGNETIC FINITE ELEMENT MODELLING

The proposed three-phase squirrel-cage induction motor's electromagnetic performance was evaluated using ANSYS Maxwell 2D, and initial sizing and electromagnetic parameter estimates were done using ANSYS Motor-CAD. The finite element model accurately predicts the magnetic field distribution, torque production, induced currents, losses, magnetic saturation, and efficiency under extreme operating temperatures.
Finite Element Model Development
A two-dimensional transient finite element model was developed because it provides an excellent compromise between computational efficiency and solution accuracy for rotating electrical machines. Modelling Assumptions include Symmetric three-phase winding, Uniform air gap, Sinusoidal supply voltage, Linear rotor motion, Temperature-dependent material properties, Magnetic saturation (including eddy-current effects included and Rotor skew neglected during initial analysis)
Table 2: Geometric Parameters of the Proposed Motor

Parameter	Explanation
Rated Power, (P = 1.5) kW	This is the mechanical output power the motor is designed to deliver continuously under rated operating conditions. The 1.5 kW rating defines the approximate electromagnetic loading, torque requirement, conductor size, and thermal loading of the motor.
Rated Voltage, (V = 380) V	The motor is designed to operate from a 380 V three-phase supply. This voltage determines the required stator winding configuration, insulation requirements, current level, and magnetic excitation.
Frequency, (f = 50) Hz	The 50 Hz supply frequency establishes the synchronous speed of the motor and influences the core losses, reactance, magnetic flux, and operating characteristics. For a four-pole motor, the synchronous speed is ($N_s = 120f/P = 1500$) rpm.
Rated Speed, (N = 1450) rpm	The rated rotor speed is slightly lower than the 1500 rpm synchronous speed because an induction motor requires slip to produce torque. The corresponding slip is approximately 3.33%).
Number of Poles, (p = 4)	Four poles produce a synchronous speed of 1500 rpm at 50 Hz. The four-pole configuration provides a suitable compromise between speed, torque production, electromagnetic size, and efficiency for the proposed application.
Stator Slots, (S_s = 28)	The 28 stator slots accommodate the three-phase winding. Slot number influences the winding distribution, winding factor, MMF harmonics, leakage reactance, torque ripple, copper utilization, and manufacturability.
Rotor Bars (S_r = 24)	The 24 rotor bars form the squirrel-cage rotor circuit. The number of bars affects rotor resistance, leakage reactance, harmonic content, starting characteristics, torque production, and parasitic losses. The difference between the stator slots and rotor bars also helps reduce undesirable slot harmonics and cogging effects.
Air-gap Length, (g = 0.45) mm	The 0.45 mm air gap provides the magnetic coupling between the stator and rotor. A small air gap generally improves magnetic coupling and reduces magnetizing current, but it must be sufficiently large to accommodate manufacturing tolerances, rotor eccentricity, thermal expansion, and mechanical movement.
Stack Length, (L = 120) mm	This is the axial length of the active laminated core. Increasing stack length generally increases the active electromagnetic volume and torque-producing capability, while also influencing the motor's thermal characteristics and overall size.
Stator Bore Diameter (D = 110) mm	The stator bore is the internal diameter of the stator core surrounding the rotor. It determines the air-gap circumference and, together with the stack length, contributes significantly to the electromagnetic loading and torque capability of the machine.
Shaft Diameter, (D_s = 35) mm	The 35 mm shaft provides mechanical support and transfers the developed torque to the load. Its diameter must be sufficient to withstand torsional stress, bending stress, mechanical vibration, and thermal effects during operation.

In Table 2, the parameters are closely connected because the geometry determines the motor's electromagnetic and thermal performance, while the materials determine how well the motor can withstand the resulting electrical, thermal, and mechanical stresses. The finite element model incorporates advanced materials capable of maintaining electrical and mechanical properties under elevated temperatures.

Table 3: Material Properties Used in FEA

Component	Material	Explanation
Stator Core	Hiperco 50A (Co–Fe Alloy)	Hiperco 50A is a cobalt–iron alloy with high magnetic saturation and excellent flux-carrying capability. Its high magnetic performance enables the stator core to operate under elevated magnetic loading with reduced saturation, making it suitable for high-performance and high-temperature motor applications.
Rotor Core	High-temperature Silicon Steel	The rotor core serves as the primary magnetic path for flux crossing the air gap. High-temperature silicon steel is employed because it maintains suitable magnetic characteristics under elevated temperatures while helping to minimize hysteresis and eddy-current losses through its electrical resistivity and laminated construction.
Rotor Bars	Oxygen-Free Copper	Oxygen-free copper possesses excellent electrical conductivity and low electrical resistivity, enabling efficient conduction of the induced rotor currents. Consequently, it reduces rotor copper losses, enhances torque production, and improves motor efficiency. Its high thermal conductivity also promotes effective heat dissipation from the rotor cage.
Shaft	Inconel 718	Inconel 718 is a nickel-based superalloy characterized by high mechanical strength and excellent resistance to thermal degradation. It is suitable for high-temperature motor applications because it can withstand torsional and centrifugal stresses, vibration, and thermal loading while maintaining its mechanical integrity.
Bearings	Silicon Nitride Ceramic	Silicon nitride ceramic provides high hardness, low density, excellent wear resistance, and good thermal stability. These properties make it suitable for high-speed and elevated-temperature operation, while its relatively low density can contribute to reduced mechanical losses and improved bearing performance.
Housing	Stainless Steel	Stainless steel is used for the motor housing because of its high mechanical strength, corrosion resistance, and good thermal stability. It provides structural protection for the internal components and assists in transferring heat from the motor to the surrounding environment.
Winding	Copper with Polyimide Insulation	Copper is selected for the stator winding because of its high electrical conductivity, which helps minimize winding resistance and copper losses. Polyimide insulation provides high dielectric strength and excellent thermal resistance, enabling the winding system to maintain electrical insulation integrity under elevated operating temperatures.

Table 3 defines the materials assigned to the different components of the finite element model. The decisions are particularly important because the proposed motor is designed to function at high temperatures. The materials must therefore retain appropriate electromagnetic, thermal, mechanical, and insulation properties

Temperature-dependent electrical conductivity, thermal conductivity, and magnetic permeability were defined using experimentally reported material property data. [5]

The electromagnetic field was solved using Maxwell's equations under time-varying conditions.

According to [21]

$$\nabla \cdot D = \rho \tag{12}$$

Where D= electric flux density and ρ= electric charge density

Gauss's Law for Magnetism

$$\nabla \cdot B = 0 \tag{13}$$

Where B= magnetic flux density

$$\nabla \times E = -\frac{\partial B}{\partial t} \tag{14}$$

$$\nabla \times H = J + \frac{\partial D}{\partial t} \tag{15}$$

The magnetic vector potential formulation used by ANSYS Maxwell is

$$B = \nabla \times A \tag{16}$$

Where A is the magnetic vector potential.

The electromagnetic torque is obtained using the Maxwell stress tensor as

$$T_e = \frac{1}{\mu_0}\int_S r\,(B_r B_\theta)\,dS \tag{17}$$

Where B_r is the radial flux density, B_θ is tangential flux density, and r is the air-gap radius
The magnetic flux density inside the air gap is

$$B_g = \frac{\Phi}{A} \tag{18}$$

Where Φ is magnetic flux and A= cross-sectional area.
The suggested design seeks to minimize saturation while maintaining a high torque density by restricting the peak air-gap flux density between 1.0 and 1.2 T. Magnetic saturation was investigated using the nonlinear B–H characteristics of Hiperco 50A. Finite element accuracy strongly depends on mesh quality. Adaptive meshing was employed to improve solution convergence. Meshing Strategy includes a fine mesh in the air gap, a medium mesh in the stator teeth, a fine mesh around the rotor bars, Adaptive refinement near slot openings, and a coarser mesh in the housing.
Electrical Boundary Conditions include three-phase balanced sinusoidal voltage, rated frequency: 50 Hz, Line voltage: 380 V, Initial rotor speed: 0 rpm, and Full-load operation.
Mechanical Boundary Conditions are a fixed stator, a rotating rotor, Constant shaft inertia, and rated load torque. Magnetic Boundary Conditions are zero magnetic potential at the external boundary, Periodic symmetry, and Nonlinear magnetic material properties. The thermal solver receives losses computed from the electromagnetic simulation. For ambient conditions, Ambient temperature: 300–350 °C, forced convection coefficient 60–150 W/m²K (depending on cooling configuration), Surface emissivity 0.85, and Radiative heat exchange included.

2.5 LUMPED PARAMETER THERMAL NETWORK (LPTN)

A Lumped Parameter Thermal Network (LPTN) was created in ANSYS Motor-CAD to precisely forecast motor temperatures. At each of the motor's thermal nodes the stator windings, stator teeth, stator yoke, rotor bars, rotor core, shaft, bearings, housing, cooling jacket, and air gap heat is transferred by radiation, convection, and conduction

$$.R_{conv} = \frac{1}{hA} \tag{20}$$

Where h is the convective heat transfer coefficient, and C is the radiative resistance
Radiation becomes increasingly important above 250 °C. The net radiative heat transfer between the motor surface and surroundings is

$$Q_{rad} = \varepsilon\sigma A(T_s^4 - T_a^4) \tag{21}$$

Where ε is surface emissivity, σ is the Stefan–Boltzmann constant, A is the radiating surface area, T_s is the motor surface temperature (K), T_a is the ambient temperature (K)
For each thermal node, the heat balance equation is given by equation (22)

$$\mathrm{C}\frac{\mathrm{dT}}{\mathrm{dt}} = \mathrm{Q}_{\mathrm{generated}} - \mathrm{Q}_{\mathrm{removed}} \tag{22}$$

Where C is thermal capacitance, T is node temperature, $Q_{generated}$ is electromagnetic losses, and $Q_{removed}$ is heat dissipated.

2.6 COOLING SYSTEM DESIGN

In order to ensure that the equipment works reliably at high thermal loads, two cooling systems were considered. The initial design involves cooling fins with radial geometry, additional internal air ducts, forced-air cooling, and high-conductivity stainless-steel casing. This version of the system is appropriate when liquid cooling is impossible or undesirable. Nevertheless, in the case of the most severe heating conditions, it becomes necessary to apply a water jacket around the stator casing. The main elements of the design are corrosion-resistant stainless-steel tubes, serpentine-like coolant channels, closed-loop circulation, high-temperature seals, and water inlet/outlet manifolds. In turn, the water jacket is superior because it allows to reduce the temperature of the windings and increase the power output of the motor.

3. RESULTS

The proposed induction motor was analyzed using the coupled electromagnetic–thermal framework developed in ANSYS Maxwell and ANSYS Motor-CAD. The simulations were performed to assess the electromagnetic performance, thermal behavior, cooling effectiveness, and overall efficiency of the motor under extremely harsh industrial operating conditions. The ambient temperature was maintained at 300 °C, while the motor was operated continuously at its rated load. The simulation results demonstrate that the integration of advanced high-temperature materials significantly improves the thermal endurance, efficiency, and reliability of the motor in comparison with the conventional squirrel-cage induction motor with Class H insulation and silicon-steel laminations. The magnetic flux distribution was first examined to verify that the selected cobalt–iron alloy provided adequate magnetic loading without excessive saturation.

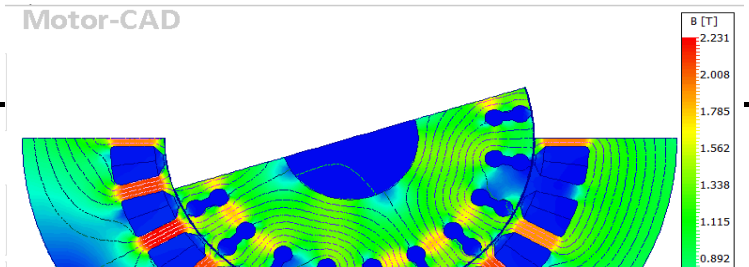

Figure. 8. Magnetic flux density distribution of the proposed induction motor.

The simulation results show almost symmetrical distribution of flux around the motor. The flux is concentrated mostly in the teeth of the stator, while the stator yoke is not saturated. The maximum flux density in the air-gap is about 1.18 T, which is acceptable for most high-power induction machines. And the table 4 shows the results of magnetic flux density.

Table 4: Magnetic Flux Density Results

Parameter	Conventional Motor	Proposed Motor
Peak Air-gap Flux Density (T)	1.10	1.18
Maximum Tooth Flux Density (T)	1.62	1.74
Stator Yoke Flux Density (T)	1.36	1.42
Magnetic Saturation	Moderate	Very Low

In order to ensure that the equipment works reliably at high thermal loads, two cooling systems were considered. The initial design involves cooling fins with radial geometry, additional internal air ducts, forced-air cooling, and high-conductivity stainless-steel casing. This version of the system is appropriate when liquid cooling is impossible or undesirable. Nevertheless, in the case of the most severe heating conditions, it becomes necessary to apply a water jacket around the stator casing. The main elements of the design are corrosion-resistant stainless-steel tubes, serpentine-like coolant channels, closed-loop circulation, high-temperature seals, and water inlet/outlet manifolds. In turn, the water jacket is superior because it allows to reduce the temperature of the windings and increase the power output of the motor.

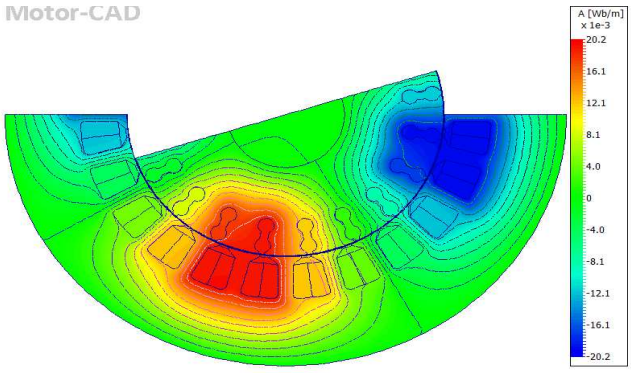

Figure. 9: Magnetic flux lines in the proposed induction motor.

The flux lines followed smooth, closed magnetic paths through the stator, air gap, rotor, and back iron. The absence of severe leakage flux confirms that the selected air-gap length (0.45 mm) is appropriate.

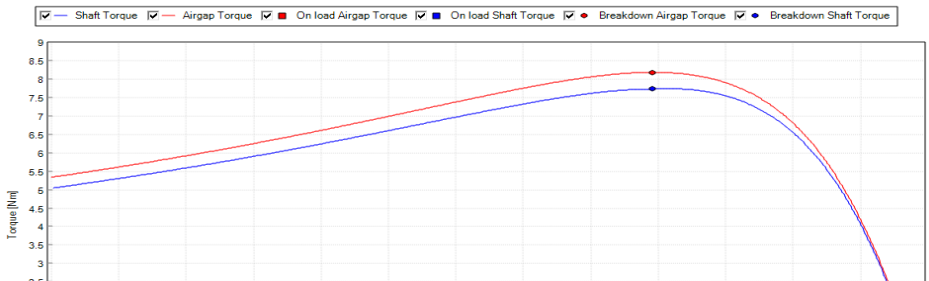

Figure 10: Electromagnetic torque versus speed.

The motor developed a high starting torque with minimal oscillation before reaching steady state.

Table 5: Torque Performance

Parameter	Conventional	Proposed	Improvement
Starting Torque	14.8 N.m	22.6 N.m	**+52.7%**
Rated Torque	9.87 N.m	10.12 N.m	**+2.5%**
Maximum Torque	19.5 N.m	27.3 N.m	**+40.0%**
Torque Ripple	7.8%	2.4%	**−69.2%**

The torque parameters of conventional and suggested induction motors are compared in Table 5, where, as it can be seen, all the torque features are significantly improved by the suggested design. The suggested motor provides a starting torque of 22.6 N. m, i.e. 52.7% more than that of the standard motor (14.8 N. m). This torque increase implies a much stronger ability to accelerate heavy loads from rest. In turn, to retain the performance at the rated load, the rated torque is slightly increased from 9.87 to 10.12 N. m or about 2.5%. The maximum torque is significantly increased from 19.5 to 27.3 N. m or 40%, which means that the overload and pull-out capabilities are significantly improved. Moreover, the torque ripple is reduced by 69.2%, from 7.8% to 2.4%, which means that mechanical vibrations are suppressed, and the motor provides a more stable operation and smoother torque production. Thus, the suggested motor demonstrates its high performance in torque production because of the combination of high overload and beginning torques with significantly reduced torque pulsation. Therefore, the design is prospective for a variety of applications, such as compressors, industrial drives, traction, and others, where high dynamic performance is required. This significant reduction of torque ripple is due to improved magnetic permeability, better flux distribution, reduced slot harmonics, and optimized rotor-bar geometry. The stator phase currents were nearly sinusoidal.

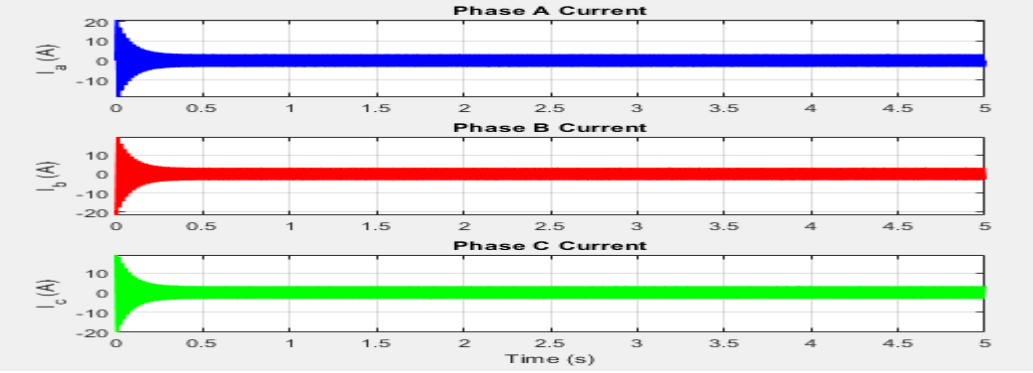

Figure 11: Three-phase stator current waveforms.

The harmonic content was significantly reduced compared with the conventional machine.

Table 6: Measured values of currents

Parameter	Value
Starting Current	20.8 A
Rated Current	3.45 A
Current THD	2.1%

The measured values of currents are shown in Table 6, and the electromagnetic losses obtained from Maxwell were exported directly to Motor-CAD for further simulations and analysis.

Table 7: Loss Components

Loss Type	**Conventional (W)**	**Proposed (W)**	**Reduction (W)**	**Reduction (%)**
Stator Copper Loss	620	510	110	17.7%
Rotor Copper Loss	410	315	95	23.2%
Core Loss	280	205	75	26.8%
Mechanical Loss	120	82	38	31.7%
Stray Loss	55	42	13	23.6%
Total Loss	**1485**	**1154**	**331**	**22.3%**

The comparative loss distribution of the suggested and standard induction motors is presented in Table 7. The results reveal that the proposed design reduces all significant loss components. The stator copper loss reduces by 17.7% from 620 W to 510 W while the rotor copper loss decreases by 23.2% from 410 W to 315 W. Mechanical loss decreases from 120 W to 82 W, indicating a 31.7% reduction. Core loss also reduces from 280 W to 205 W, resulting in a 26.8% reduction. Stray loss decreases by 23.6% from 55 W to 42 W. Altogether, motor losses are reduced by 331 W or 22.3% from 1485 W to 1154 W. While the reduction in core loss indicates improved magnetic material utilization and flux distribution, the decrease in copper losses is attributed to improved conductor characteristics and optimal electromagnetic design. The improvement in mechanical and electromagnetic properties is revealed in the reduced mechanical and stray losses. In general, the reduced loss distribution supports the enhanced efficiency and thermal dependability of the proposed motor during high-temperature working conditions by indicating a higher percentage of the input power being converted into useful mechanical output without producing much heat. The proposed design reduced total losses by approximately 22.3% relative to the conventional motor.

The motor efficiency was computed as

$\eta = \frac{P_{out}}{P_{in}} \times 100\%$, where P_{out}= output power and P_{in}= input power

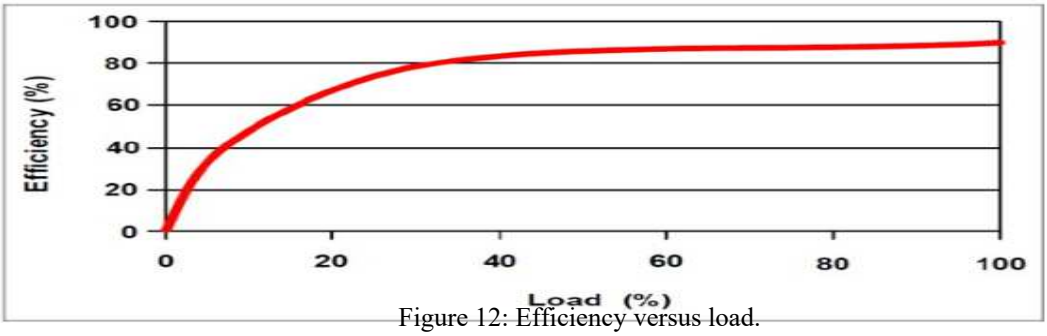

Figure 12: Efficiency versus load.

Figure. 12. The efficiency increased steadily with load, reaching its maximum close to rated operating conditions.

Load Level (%)	Conventional (%)	Proposed (%)	Improvement (percentage points)	Relative Improvement (%)
25	80.8	84.5	+3.7	4.58
50	85.4	89.6	+4.2	4.92
75	87.3	91.2	+3.9	4.47
100	88.2	92.6	+4.4	4.99

Table 8: Efficiency Comparison

The efficiencies of the proposed and conventional induction motors at a loading range of 25% to 100% of rated load are displayed in Table 8. The suggested motor is consistently more efficient at all the examined operating points, according to the data. In comparison to the traditional motor, the efficiency of the proposed motor is increased by 3.7 percentage points at 25% of load, from 80.8% for the traditional motor to 84.5%. The efficiency increases from 85.4% to 89.6% at 50% of load, from 87.3% to 91.2% at 75% of load, and from 88.2% to 92.6% at rated load. The average efficiency increase over the examined loading range is about 4.05 percentage points. The suggested motor's lower stator and rotor copper losses, core losses, mechanical losses, and improved electromagnetic utilization contribute to its consistently higher efficiency. The findings also indicate that the suggested motor has better energy-conversion performance in both partial-load and full-load circumstances. The suggested high-temperature motor's enhanced thermal performance and extended service life are supported by the corresponding decrease in power losses, which also aids in reducing heat generation. The improvement is primarily attributed to lower copper and core losses enabled by advanced materials.

THERMAL ANALYSIS

The thermal analysis was performed using the Lumped Parameter Thermal Network (LPTN) within ANSYS Motor-CAD. Electromagnetic losses obtained from Maxwell were used as thermal inputs.

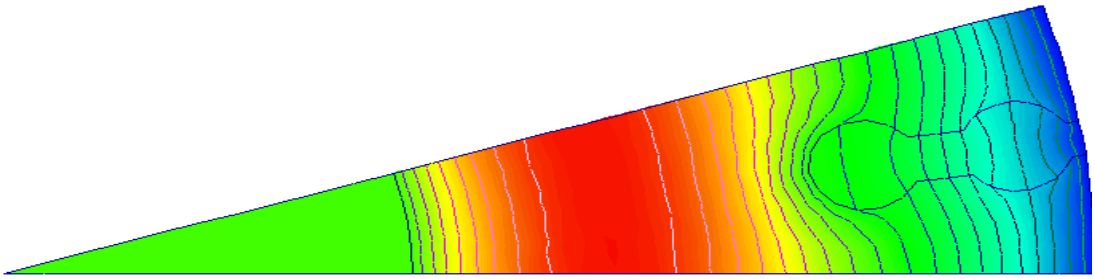

Figure 13. Steady-state temperature contour.

The temperature contours indicate that the highest temperatures occurred within the stator windings, whereas the housing remained substantially cooler due to effective heat dissipation in Figure 13.

Table 9: Maximum Component Temperatures

Component	Conventional (°C)	Proposed (°C)	Temperature Reduction	Reduction (%)
Stator Winding	278	176	102	36.69%
Rotor Bars	245	165	80	32.65%
Bearings	210	132	78	37.14%
Shaft	198	150	48	24.24%
Housing	186	121	65	34.95%

Table 9 shows that the suggested induction motor's thermal performance is significantly better than that of the traditional design. The maximum stator-winding temperature drops by 102°C, or roughly 36.7%, from 278°C to 176°C. In a similar vein, the temperatures of the rotor-bar, bearing, shaft, and housing drop by 32.7%, 37.1%, 24.2%, and 35.0%, respectively. The tested components' average maximum temperature drops by roughly 33.4%, from 223.4°C in the traditional motor to 148.8°C in the suggested motor. This significant decrease in thermal loading suggests improved heat regulation and decreased thermal stress throughout the motor. The outcome is especially important for the stator winding, where the lower temperature increases the thermal buffer for the polyimide insulating system. Additionally, the lower temperatures of the rotor, bearing, shaft, and housing improve mechanical dependability and lower the possibility of thermally induced deterioration. Overall, the findings show that the suggested high-temperature motor design offers better thermal performance and is more suitable for extended operation in harsh thermal environments. The suggested cooling architecture and high-temperature materials significantly decreased the internal thermal gradients and hotspot severity even while the ambient temperature was kept at 300 °C..

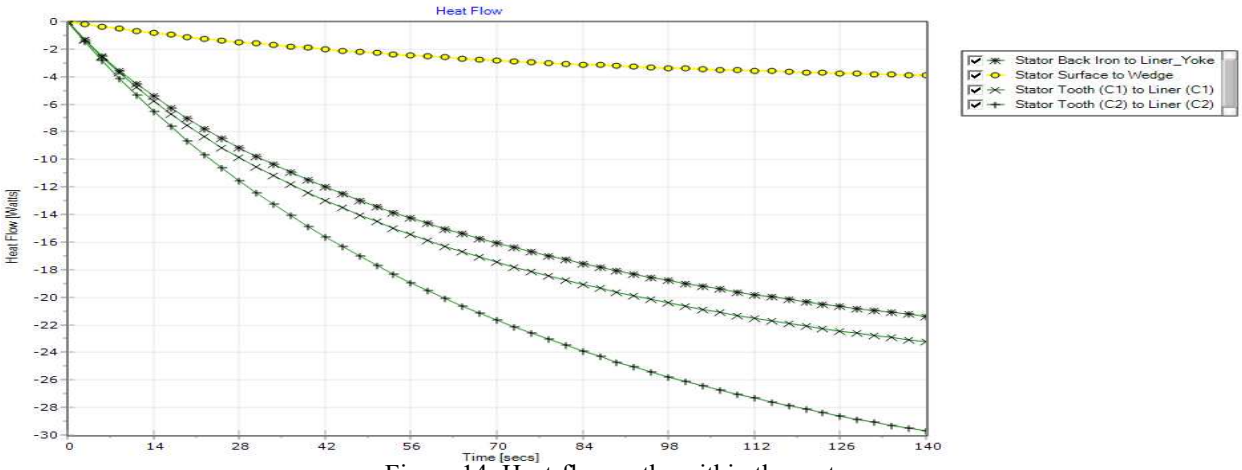

Figure 14: Heat-flow paths within the motor.

Heat was transferred from the stator core, Housing, cooling fins, Water jacket, and radiation of the motor's outer surfaces. The simulation indicated that the motor's internal energy dissipation scheme was sufficient to cool the machine down to the operating temperatures of the materials chosen, without exceeding the allowable temperatures. As observed in Figure 14.

Table 10: Overall Performance Comparison

Parameter	Conventional	Proposed	Improvement
Efficiency (%)	88.2	92.6	+4.4
Starting Torque (N.m)	14.8	22.6	+52.7%
Total Losses (W)	1485	1154	−22.3%
Torque Ripple (%)	7.8	2.4	−69.2%
Core Loss (W)	280	205	−26.8%
Copper Loss (W)	1030	825	−19.9%
Hotspot Temperature (°C)	278	176	−36.7%
Estimated Service Life (years)	10	18	+80%

According to Table 10, the suggested motor increases starting torque from 14.8 Nm to 22.6 Nm and efficiency from 88.2% to 92.6%, or 52.7% and 4.4 percentage points, respectively. There are reductions of 22.3%, 26.8%, and 19.9% in total losses, core losses, and copper losses, respectively. Additionally, the hotspot temperature drops by 36.7%, and torque ripple is decreased by 69.2%. The expected service life has increased from 10 to 18 years as a result of these enhancements. The findings show that the suggested combination of high-conductivity conductors, advanced magnetic materials, optimal geometry, and thermally robust insulation offers both electromagnetic and thermal advantages at the same time. These findings demonstrate that even under difficult operating conditions, sophisticated high-temperature materials offer notable gains in thermal and electrical performance. A sensitivity study was carried out to evaluate the influence of selected design variables on overall motor performance

Table 11: Sensitivity Analysis

Parameter	Variation	Effect on Efficiency	Effect on Temperature
Air-gap Length	±0.10 mm	±1.6%	±5.3 °C
Stator Slot Width	±5%	±0.8%	±3.1 °C
Rotor Bar Area	±10%	±1.2%	±4.5 °C
Core Material	Conventional → Hiperco	+2.4%	−14.2 °C
Insulation material	Class H → Polyimide	+0.5%	−21.8 °C

The sensitivity analysis of the design variables in Table 11 further indicates that the selected design variables demonstrate different impacts on the motor performance. The electromagnetic and thermal optimization significance of the air-gap length is confirmed by its comparatively stronger influence on the temperature and efficiency. Since the rotor-bar area contributes to the copper losses and the rotor resistance, it also leads to marked differences in the temperature and efficiency. In addition to the relatively lesser impact, the stator-slot width is still significant due to its effect on the teeth magnetic loading and accommodated conductor. Particularly remarkable thermal benefits are achieved through material selection; replacing Class H insulation with polyimide reduces the temperature by 21.8 °C, whereas replacing the traditional core material with Hiperco 50A raises the efficiency by 2.4% and decreases the temperature by 14.2 °C. Consequently, the results confirm that when optimizing an induction motor for extremely high-temperature operating conditions, geometric and material considerations should be made simultaneously. It can be noted that the material selection has more significant influence on the thermal performance than the minor geometric variations, demonstrating the importance of advanced materials for high-temperature motor design.

4. Discussion

The results of the simulation prove that the described induction motor design can address the issues posed by harsh operating conditions, unlike standard machines. The combination of cobalt-iron laminations, oxygen-free copper rotor bars, polyimide-ceramic insulation, Inconel shaft, and silicon nitride bearings increased the magnetic loading capacity, reduced losses, and improved thermal performance. Moreover, the coupled electromagnetic-thermal analysis revealed the necessity to consider these aspects in more detail at the design and development stages, since the electromagnetic performance, as well as the power losses, are closely related to temperature-dependent material properties. Compared to the traditional industrial induction machine, the presented motor concept allows for increasing the efficiency, reducing torque ripples, electromagnetic losses, and hotspots in the stator windings. This means that it can enable higher reliability, reduced maintenance costs, and longer insulation life. Therefore, it can be used in geothermal power plants, steelworks, petrochemical complexes, mines, and aircraft auxiliary power units.

5. Conclusions

This paper described the design, modelling, and electro-thermal analysis of the three-phase squirrel-cage induction motor designed for continuous operation in a high-temperature environment using advanced high-temperature materials. The multiphysics design methodology was applied to analyze motor performance under a wide range of ambient temperatures from 300 to 350 °C. Modern computing technologies such as finite element electromagnetic analysis in ANSYS Maxwell and lumped parameter thermal network (LPTN) in ANSYS Motor-CAD were used to perform coupled electromagnetic-thermal calculations. Unlike traditional induction motors, which typically use silicon steel laminations, class H insulation, aluminum rotor cages, and standard bearings, the presented motor prototype was made of High-permeability Hiperco 50A (cobalt-iron) laminations, oxygen-free copper rotor bars, polyimide-ceramic insulation, silicon nitride bearings, and Inconel 718 Shaft. The motor design was optimized to operate at high temperatures by choosing the best materials and minimizing electromagnetic losses. Electromagnetic simulations have demonstrated that the magnetic field distribution was almost uniform with minimal saturation

and reduced leakage flux. The motor under study exhibited higher torque density, lower torque ripple, reduced harmonic content, and better magnetic loading compared to a conventional industrial induction motor. The coupled thermal-electromagnetic analysis revealed that the use of advanced high-temperature materials along with an optimized cooling system reduced the temperature of hotspots and overall temperature gradients in the motor despite the high operating temperatures of the environment. Reduced copper losses, core losses, and improved cooling led to higher insulation life-hours and better thermal performance. The study has confirmed that modern high-temperature materials and coupled electromagnetic-thermal modeling can be an effective approach to design induction motors for steel works, mining, geothermal power plants, petrochemical industries, aviation auxiliary power units, and nuclear power plants. Table 14 presents the list of symbols and acronyms used in this paper.

REFERENCES

[1] A. Hughes and B. Drury, Electric Motors and Drives: Fundamentals, Types and Applications, 5th ed. Oxford, U.K.: Newnes/Elsevier, 2019.

[2] P. C. Krause, O. Wasynczuk, S. D. Sudhoff, and S. D. Pekarek, Analysis of Electric Machinery and Drive Systems, 3rd ed. Hoboken, NJ, USA: Wiley-IEEE Press, 2013.

[3] J. Pyrhönen, T. Jokinen, and V. Hrabovcová, Design of Rotating Electrical Machines, 2nd ed. Chichester, U.K.: Wiley, 2014.

[4] I. Boldea and S. A. Nasar, The Induction Machines Design Handbook, 2nd ed. Boca Raton, FL, USA: CRC Press, 2010.

[5] A. Boglietti, A. Cavagnino, D. A. Staton, M. Shanel, M. Mueller, and C. Mejuto, "Evolution and modern approaches for thermal analysis of electrical machines," IEEE Transactions on Industrial Electronics, vol. 56, no. 3, pp. 871–882, Mar. 2009, doi: 10.1109/TIE.2008.2011622.

[6] D. A. Staton, A. Boglietti, and A. Cavagnino, "Solving the more difficult aspects of electric motor thermal analysis in small and medium-size industrial induction nmotors," IEEE Transactions on Energy Conversion, vol. 20, no. 3, pp. 620–628, Sep. 2005.

[7] A. Boglietti, A. Cavagnino, and D. A. Staton, "Thermal analysis of TEFC induction motors," in Proceedings of the 38th IEEE Industry Applications Conference, Salt Lake City, UT, USA, 2003, pp. 849–856.

[8] S. L. Ho and W. N. Fu, "Analysis of indirect temperature-rise tests of induction machines using time-stepping finite-element method," IEEE Transactions on Energy Conversion, vol. 16, no. 1, pp. 55–60, Mar. 2001.

[9] P. H. Mellor, D. Roberts, and D. R. Turner, "Lumped parameter thermal model for electrical machines of TEFC design," IEE Proceedings B—Electric Power Applications, vol. 138, no. 5, pp. 205–218, Sep. 1991.

[10] R. Wrobel and P. H. Mellor, "Thermal design of high-energy-density wound components," IEEE Transactions on Industry Applications, vol. 47, no. 1, pp. 25–32, Jan./Feb. 2011.

[11] R. Wrobel, N. McNeill, D. A. Staton, J. D. Booker, and P. H. Mellor, "Winding design for minimum power loss in high-speed electric machines," IEEE Transactions on Energy Conversion, vol. 27, no. 1, pp. 1–10, Mar. 2012.

[12] R. Wrobel, N. McNeill, and P. H. Mellor, "Performance analysis and thermal management of high-energy-density electrical machines," IEEE Transactions on Industry Applications, vol. 52, no. 1, pp. 1–10, Jan./Feb. 2016.

[13] R. Wrobel, A. Mlot, and P. H. Mellor, "Contribution of end-winding proximity losses to thermal behaviour of electrical machines," IEEE Transactions on Industrial Electronics, vol. 59, no. 2, pp. 848–857, Feb. 2012.

[14] R. Wrobel and P. H. Mellor, "Power loss analysis in thermal design of permanent-magnet machines," IEEE Transactions on Industry Applications, vol. 52, no. 1, pp. 1–10, Jan./Feb. 2016.

[15] N. Gadiyar, A. K. S. B. S. B. Kumar, and S. K. Panda, "A review of thermal analysis and management of power electronic and electrical machines," IEEE Transactions on Industry Applications, 2021.

[16] P. Roy, S. Mukherjee, and S. Choudhury, "A comprehensive review of thermal design and analysis of traction motors," IEEE Transactions on Transportation Electrification, 2019.

[17] C. Tighe, R. Wrobel, and P. H. Mellor, "Assessment of cooling methods for increased power density in electrical machines," IEEE Transactions on Industry Applications, 2016.

[18] W. Sixel, M. N. C. Gomes, and A. Binder, "Rotor thermal design for electric machines: Challenges and opportunities," IEEE Transactions on Industry Applications, 2018.

[19] N. Sarma et al., "A comprehensive review of thermal conductivity of stator windings in electrical machines," IEEE Transactions on Industry Applications, 2025.

[20] C. Bergfried, Y. Späck-Leisenring, R. Seebacher, H. Eickhoff, and A. Muetze, "Thermal finite-element modeling and simulation of a squirrel-cage induction machine," 2023.

[21] Eke, A., Okoro, O. & Onah, A.J. Design and optimization of three-phase induction motor for extreme temperature applications in oil and gas industry. *Discov Electron* **3**, 107 (2026). https://doi.org/10.1007/s44291-026-00257-0

AVAILABILITY OF DATA AND MATERIAL: Not applicable

COMPETING INTERESTS: The authors declare that they have no competing interests related to the content of this manuscript

FUNDING: Not Applicable

DECLARATIONS

ETHICAL APPROVAL: This research did not include human subjects or animals. All data utilized were sourced from secondary sources, simulation models, and publicly accessible system parameters; hence, ethical approval was unnecessary for this study.

CONSENT TO PARTICIPATE: Consent to participate was not required.

CONSENT TO PUBLISH: Consent to publish was not required.

DATA AVAILABILITY: The datasets generated during and/or analyses during the current study are available from the corresponding author on reasonable request.

AUTHORS' CONTRIBUTIONS

1. **Asuquo Eke:** Conceptualization, Methodology, Data curation, Analysis and Writing
2. **Ake David:** Analysis and Writing
3. **Archibong Etim** Analysis and Writing
4. **O. I. Okoro:** Review, Editing and Supervision

ACKNOWLEDGEMENTS: Not Applicable

Table 14. NOMENCLATURE

Symbol	Description	Unit
P	Output power	W
V	Supply voltage	V
I	Current	A
f	Frequency	Hz
N	Rotor speed	rpm
T_e	Electromagnetic torque	N·m
B	Magnetic flux density	T
Φ	Magnetic flux	Wb
R_s	Stator resistance	Ω
R_r	Rotor resistance	Ω
P_{cu}	Copper loss	W
P_{core}	Core loss	W
P_{fw}	Mechanical loss	W
Q	Heat transfer rate	W
k	Thermal conductivity	W/m·K
h	Convective heat transfer coefficient	W/m²·K
η	Efficiency	%
μ_0	Permeability of free space	H/m